Quaternary Science Reviews 93 (2014) 142–154

Contents lists available at ScienceDirect

Quaternary Science Reviews

journal homepage: www.elsevier.com/locate/quascirev

Mid- to Late-Holocene Australian–Indonesian summer monsoon variability

Stephan Steinke [a,*], Mahyar Mohtadi [a], Matthias Prange [a], Vidya Varma [a,1], Daniela Pittauerova [b], Helmut W. Fischer [b]

[a] MARUM –Center for Marine Environmental Sciences and Department of Geosciences, University of Bremen, 28359 Bremen, Germany
[b] Bremen State Radioactivity Measurements Laboratory, Institute of Environmental Physics (IUP), University of Bremen, 28359 Bremen, Germany

A R T I C L E I N F O

Article history:
Received 10 December 2013
Received in revised form
31 March 2014
Accepted 4 April 2014
Available online 4 May 2014

Keywords:
Australian–Indonesian summer monsoon
Holocene
Orbital forcing
Solar forcing
Grand solar minimum

A B S T R A C T

The Australian–Indonesian monsoon has a governing influence on the agricultural practices and livelihood in the highly populated islands of Indonesia. However, little is known about the factors that have influenced past monsoon activity in southern Indonesia. Here, we present a ~6000 years high-resolution record of Australian-Indonesian summer monsoon (AISM) rainfall variations based on bulk sediment element analysis in a sediment archive retrieved offshore northwest Sumba Island (Indonesia). The record suggests lower riverine detrital supply and hence weaker AISM rainfall between 6000 yr BP and ~3000 yr BP compared to the Late Holocene. We find a distinct shift in terrigenous sediment supply at around 2800 yr BP indicating a reorganization of the AISM from a drier Mid Holocene to a wetter Late Holocene in southern Indonesia. The abrupt increase in rainfall at around 2800 yr BP coincides with a grand solar minimum. An increase in southern Indonesian rainfall in response to a solar minimum is consistent with climate model simulations that provide a possible explanation of the underlying mechanism responsible for the monsoonal shift. We conclude that variations in solar activity play a significant role in monsoonal rainfall variability at multi-decadal and longer timescales. The combined effect of orbital and solar forcing explains important details in the temporal evolution of AISM rainfall during the last 6000 years. By contrast, we find neither evidence for volcanic forcing of AISM variability nor for a control by long-term variations in the El Niño-Southern Oscillation (ENSO).

1. Introduction

The Asian and Australasian monsoons affect roughly half the world's population, which largely depends on the monsoonal climate for their food and livelihood (Webster et al., 1998; Christensen et al., 2007). Despite the importance to so many, the monsoon is difficult to predict and model, making its future development in a changing global climate uncertain (Webster et al., 1998). Hence, it is vital to reconstruct monsoon variations beyond the instrumental record in order to improve our understanding of the mechanisms that may act on monsoonal rainfall variability. Most proxy evidence on multi-decadal to multi-millennial scale changes in monsoonal rainfall intensity during the Holocene has been deduced from continental and marine archives located in the Indian and East Asian monsoon domains. These studies on the Indian (Fleitmann et al., 2003; Gupta et al., 2005) and the East Asian (Wang et al., 2005; Zhang et al., 2008) summer monsoon rainfall indicate a strong response to orbital and solar forcing during the Holocene. In contrast to its Northern Hemisphere counterparts, very little is known about the development of the Australian-Indonesian summer monsoon (AISM) rainfall during the Holocene.

With respect to the AISM rainfall during the Holocene, Australian proxy records suggest wetter conditions during the Early and Mid Holocene compared to present (Nott and Price, 1994; Magee et al., 2004) which has been explained by a Northern Hemisphere insolation control (Magee et al., 2004; Miller et al., 2005), a response to regional sea-surface temperatures (Liu et al., 2003) or human-induced changes in vegetation cover during the Late Holocene (Miller et al., 2005). In contrast, two recent studies from southern Indonesia indicate reduced rainfall during the Mid Holocene compared to the Late Holocene (Griffiths et al., 2009; Mohtadi et al., 2011), highlighting the complex and contrasting patterns of AISM development in southern Indonesia and northern

* Corresponding author.
E-mail address: ssteinke@uni-bremen.de (S. Steinke).
[1] Now at the Department of Meteorology, Stockholm University, SE-10691 Stockholm, Sweden.

http://dx.doi.org/10.1016/j.quascirev.2014.04.006
0277-3791/

Australia. Another study relates the changes in AISM rainfall during the past two millennia to shifts in the mean position of the Inter-Tropical Convergence Zone (ITCZ) forced by variations in Northern Hemisphere climate mean state (Tierney et al., 2010). A recent study from the Australian tropics suggests that El Niño-Southern Oscillation (ENSO) may have played a dominant role in driving AISM variability since the middle Holocene (Denniston et al., 2013). Taken together, mechanisms that influence the AISM during the Holocene are far from being understood because of the limited number of AISM records and the strong disagreement on the nature and causes of rainfall changes in the existing AISM records.

Here, we present a ~6000 years high-resolution record of southern Indonesian rainfall based on bulk sediment element analysis in a sediment archive retrieved offshore northwest Sumba Island (Indonesia). This new record allows us to study the history of monsoonal rainfall in southern Indonesia at multi-decadal to multi-millennial time scales, and to explore the role of various potential forcing mechanisms in driving AISM rainfall through the Holocene.

2. Modern climate

At present, south and central Indonesia from south Sumatra to Timor Island, parts of Kalimantan, Sulawesi, and Irian Jaya as well as the northern portions of Australia experience a monsoonal climate, with the majority of the annual rainfall occurring in austral summer (December–March) when the northwest monsoon carries humid air and heavy rainfall as the ITCZ-related rainbelt migrates southward (Fig. 1a). During austral winter (June–September), the southeast monsoon winds are relatively cool and dry while the ITCZ is located over mainland Asia. The annual rainfall in the study area is highest during the summer wet season (~6.5 mm/day; December–March) and negligible during the winter dry season (~0.3 mm/day; June–September; Fig. 1b). On interannual time-scales, rainfall in southern Indonesia is highly sensitive to ENSO (e.g. Webster et al., 1998; Aldrian and Susanto, 2003) with El Niño events typically resulting in reduced rainfall and subsequent drought while increased rainfall and severe floods are associated with La Niña events over much of central and southern Indonesia.

3. Strategy and proxy variables used for rainfall reconstruction

We use the logarithmic ratio between titanium (Ti) and calcium (Ca) as a proxy for riverine terrestrial input as in Mohtadi et al. (2011). The linkage between riverine detrital input and AISM rainfall has been demonstrated previously for the study area by Rixen et al. (2006). The supply of terrigenous material as monitored by the ratio between the lithogenic particles and calcium carbonate

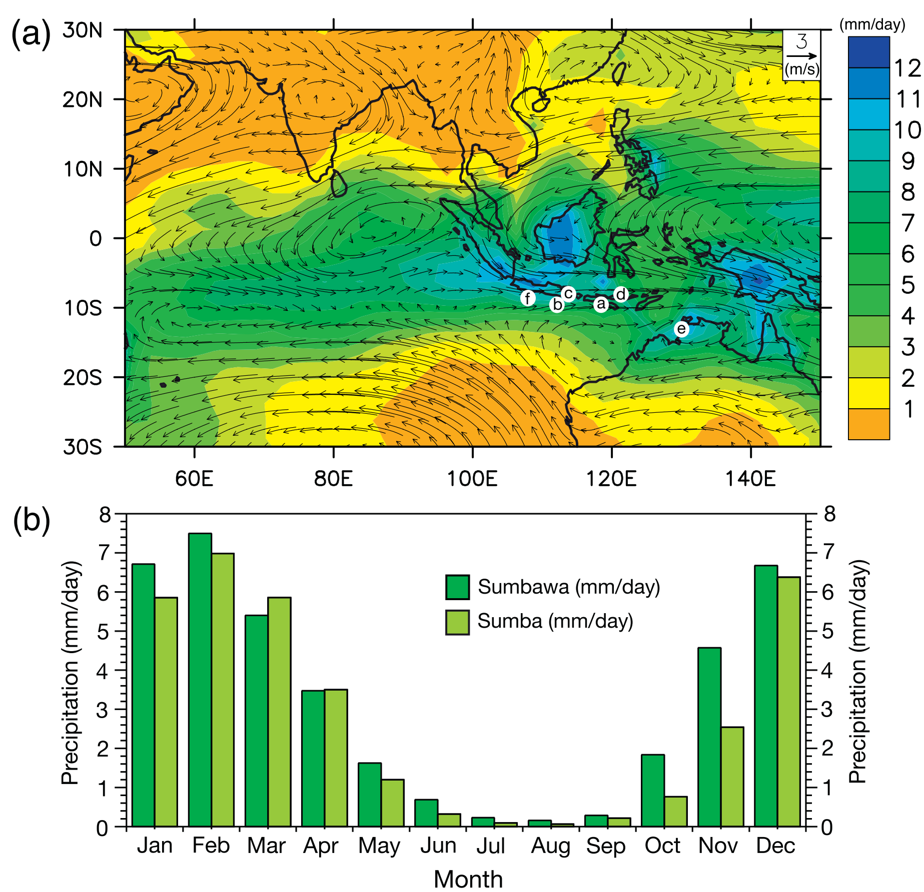

Fig. 1. (a) Precipitation and 850-hPa wind climatologies (1981–2010) for the austral summer season (December–February) in the Asian–Australian monsoon region. Data sets are Global Prediction Climatology Project (GPCP) version 2.2 for precipitation (Adler et al., 2003) and NCEP/NCAR reanalysis for wind (Kalnay et al., 1996). Other records of Australian–Indonesian summer monsoon (AISM) variability discussed in the text are also indicated: (a) Ti/Ca ratios in core GeoB10065-7 (this study), (b) Ti/Ca ratios in core GeoB10053-7 (Mohtadi et al., 2011); (c) Lake Lading leaf wax δD record (Konecky et al., 2013); (d) Liang Luar stalagmite $\delta^{18}O$ record (Griffiths et al., 2010); (e) Kimberley stalagmite $\delta^{18}O$ record (Denniston et al., 2013). (f) Indicates the position of sediment trap JAM off south Java (Rixen et al. (2006)); (b) Monthly average rainfall between 1998 and 2010 for Sumbawa (114.5–119.2°E; 9.15–8.15°S) and Sumba (118.5–120.5°E; 10.15–9.15°S) derived from the Tropical Rainfall Measuring Mission (TRMM; http://trmm.gsfc.nasa.gov) and the Global Precipitation Climatology Centre (GPCC; Deutscher Wetterdienst; http://dwd.de) precipitation 0.25° dataset interpolatd via http://climexp.knmi.nl.

Table 1
MUC-A GeoB10065-9 chronology.

Depth cm	Corrected depth cm	Activity $Bq \cdot kg^{-1}$	Uncert. $Bq \cdot kg^{-1}$	CF-CS model		CRS model	
				Calendar yr (AD)	Sed. rate $cm \cdot yr^{-1}$	Calendar yr (AD)	Sed. rate $cm \cdot yr^{-1}$
3.5–11.5[a]	5.5–13.5[a]						
12.5	14.5	1094	92	2009 ± 7	0.27 ± 0.02	2004 ± 6	0.27 ± 0.03
13.5	15.5	859	73	2005 ± 7	0.27 ± 0.02	2000 ± 6	0.31 ± 0.03
14.5	16.5	841	72	2001 ± 6	0.27 ± 0.02	1996 ± 6	0.28 ± 0.03
15.5	17.5	719	63	1997 ± 6	0.27 ± 0.02	1992 ± 6	0.30 ± 0.03
16.5	18.5	535	50	1994 ± 6	0.27 ± 0.02	1989 ± 6	0.36 ± 0.04
17.5	19.5	546	51	1990 ± 6	0.27 ± 0.02	1986 ± 6	0.32 ± 0.04
18.5	20.5	572	52	1986 ± 6	0.27 ± 0.02	1983 ± 6	0.27 ± 0.04
19.5	21.5	540	49	1982 ± 6	0.27 ± 0.02	1979 ± 6	0.26 ± 0.04
20.5	22.5	539	53	1978 ± 5	0.27 ± 0.02	1975 ± 6	0.23 ± 0.04
21.5	23.5	401	38	1974 ± 5	0.27 ± 0.02	1970 ± 7	0.26 ± 0.04
22.5	24.5	342	35	1970 ± 5	0.27 ± 0.02	1966 ± 7	0.27 ± 0.05
23.5	25.5	226	30	1966 ± 5	0.27 ± 0.02	1962 ± 8	0.36 ± 0.08
24.5	26.5	201	24	1962 ± 5	0.27 ± 0.02	1959 ± 8	0.37 ± 0.08
25.5.	27.5	182	21	1958 ± 5	0.27 ± 0.02	1956 ± 8	0.38 ± 0.08
26.5	28.5	200	23	1954 ± 5	0.27 ± 0.02	1953 ± 9	0.31 ± 0.08
27.5	29.5	202	29	1950 ± 5	0.27 ± 0.02	1950 ± 10	0.28 ± 0.08
28.5	30.5	162	20	1946 ± 5	0.27 ± 0.02	1946 ± 10	0.31 ± 0.09
29.5	31.5	199	25	1942 ± 5	0.27 ± 0.02	1943 ± 11	0.23 ± 0.08
Extrapolation to GC 10065-7:							
1				1984 ± 6	0.27 ± 0.02		
15				1928 ± 5	0.27 ± 0.02		
36				1845 ± 9	0.27 ± 0.02		

[a] The $^{210}Pb_{xs}$ data of MUC-A and MUC-B reveal the existence of a 10-cm thick sequence of repeated young sediment above 14 cm corrected depth. This can likely be attributed to small-scale deformation and/or sliding processes due to seismic activity that can often occur in an earthquake prone region like Indonesia.

in a sediment trap off South Java (JAM; see Fig. 1a for location) shows pronounced seasonal variations with higher terrestrial supply during the austral summer monsoon season (Rixen et al., 2006). Furthermore, river discharge, for example in eastern Java is highest during the summer monsoon season and only minor during the winter season (Jennerjahn et al., 2004). The distinct seasonality of precipitation, river discharge, and lithogenic fluxes in the water column suggests that the terrigenous fraction of the sediments off South Java is coupled to onshore precipitation during the austral summer monsoon season. By analogy, we assume the same monsoonal variations in precipitation and terrestrial supply in our study area in the eastern Lombok Basin northwest off Sumba Island. Thus, downcore variations in the logarithmic ratio between Ti and Ca are interpreted as a measure of past changes in summer monsoon rainfall. The use of the Ti/Ca ratio as a measure for riverine terrestrial input is further justified by the fact that variations in the Ti/Ca ratio determined by X-ray fluorescence and in the lithogenic/$CaCO_3$ ratio from the bulk sediment analysis in core GeoB10053-7 off South Java show a strong correlation over the last 22,000 years (Mohtadi et al., 2011).

4. Material and methods

4.1. Core GeoB10065-7

Sediment core GeoB10065-7 (9°13.39′S; 118°53.58′E; 1296 m water depth; core length 9.75 m) was recovered from the eastern Lombok Basin – northwest off Sumba Island and southeast off Sumbawa Island (Indonesia), during the RV SONNE SO-184 "PABESIA" expedition in 2005 (Fig. 1a). Sedimentological description of the core revealed dark olive grey to olive grey nannofossil/diatom-bearing clay (Hebbeln et al., 2006). A turbidite layer has been identified between 37 and 40 cm depth in the core. Age control for gravity core GeoB10065-7 is based on excess ^{210}Pb, an anthropogenic fallout radionuclide ^{241}Am and Accelerator Mass Spectrometry (AMS) radiocarbon dates. Two parallel multi-cores GeoB10065-9 (9°13.41′S; 118°53.55′E; 1284 m water depth, core length 0.6 m) were also ^{210}Pb dated in order to better constrain the age chronology of the upper 15 cm of gravity core GeoB10065-7 which is also based on ^{210}Pb dating (see below).

4.2. ^{210}Pb dating

^{210}Pb dating was used to establish the age model for the top 15 cm for gravity core GeoB10065-7 (Table 1). The freeze-dried sediment samples were analyzed by low-level gamma spectroscopy (analyzed at the Bremen State Radioactivity Measurements Laboratory, Institute of Environmental Physics, University of Bremen). A coaxial HPGe detector Canberra Industries (50% relative efficiency) housed in a 10 cm Pb shielding with Cu, Cd and plastic lining operated under Genie 2000 software was used. The efficiencies have been calculated using LabSOCS© (Laboratory SOurceless Calibration System), Genie 2000 software calibration tool. For determination of excess-^{210}Pb activity ($^{210}Pb_{xs}$), ^{210}Pb (supported) activity was subtracted from the ^{210}Pb (total) signal. Supported ^{210}Pb was derived from the concentration of ^{226}Ra measured via its daughter products ^{214}Pb and ^{214}Bi. Additionally, the artificial isotopes ^{137}Cs and ^{241}Am were analyzed. All data are related to sample dry mass.

4.3. Radiocarbon dating

Due to the lack of sufficient specimens for mono-specific planktonic foraminifera samples, Accelerator Mass Spectrometry (AMS) ^{14}C-datings were performed on mixed samples (9–20 mg) of mixed layer and thermocline dwelling planktonic foraminifera (analyzed at the National Ocean Sciences Accelerator Mass Spectrometry Facility, Woods Hole, USA and the Keck Carbon Cycle Accelerator Mass Spectrometry Laboratory, University of California, Irvine, USA; Table 2). Radiocarbon dates were converted to 2σ calendar ages with

Table 2
AMS-^{14}C ages and cal. ages of core GeoB10065-7.

Lab. code	Sample depth (cm)	Foraminifera species	^{14}C age (yr BP)	Cal. age BP	2σ cal. age range[c] (Relative area under probability distribution)
NOSAMS-OS-64679[a]	8	*Mixed planktonic foraminifera*	415 ± 30	[d]	[d]
NOSAMS-OS-81188[a]	27	*Mixed planktonic foraminifera*	690 ± 25	90	0–153 (0.817) 157–228 (0.183)
UCIAMS-89139[b]	36	*G. ruber* + *G. sacculifer*	630 ± 20	120[e]	0–30 (0.078) 40–236 (0.887)
UCIAMS-84721[b]	41	*Mixed planktonic foraminifera*	755 ± 20	170	0–24 (0.043) 48–270 (0.957)
NOSAMS-OS-73005[a]	53	*Mixed planktonic foraminifera*	970 ± 75	390	238–531 (1.0)
NOSAMS-OS-81189[a]	77	*Mixed planktonic foraminifera*	890 ± 30	320	152–158 (0.004) 227–453 (0.996)
NOSAMS-OS-64680[a]	103	*Mixed planktonic foraminifera*	935 ± 30	360	271–460 (1.0)
NOSAMS-OS-81229[a]	127	*Mixed planktonic foraminifera*	1050 ± 25	460	335–345 (0.012) 355–532 (0.988)
NOSAMS-OS-72100[a]	158	*Mixed planktonic foraminifera*	1340 ± 30	680	565–580 (0.015) 590–776 (0.985)
NOSAMS-OS-81230[a]	182	*Mixed planktonic foraminifera*	1410 ± 25	730	651–854 (1.0)
NOSAMS-OS-64681[a]	213	*Mixed planktonic foraminifera*	1530 ± 35	850	727–957 (1.0)
NOSAMS-OS-81232[a]	232	*Mixed planktonic foraminifera*	1650 ± 25	980	885–1109 (1.0)
NOSAMS-OS-72101[a]	263	*Mixed planktonic foraminifera*	1800 ± 30	1140	1020–1257 (1.0)
NOSAMS-OS-81231[a]	284	*Mixed planktonic foraminifera*	1900 ± 25	1240	1136–1331 (1.0)
NOSAMS-OS-64750[a]	308	*Mixed planktonic foraminifera*	1960 ± 35	1290	1179–1394 (1.0)
NOSAMS-OS-81233[a]	334	*Mixed planktonic foraminifera*	2140 ± 30	1470	1343–1598 (1.0)
NOSAMS-OS-72102[a]	358	*Mixed planktonic foraminifera*	2280 ± 30	1630	1515–1773 (1.0)
NOSAMS-OS-81234[a]	377	*Mixed planktonic foraminifera*	2400 ± 30	1770	1627–1895 (1.0)
NOSAMS-OS-64751[a]	403	*Mixed planktonic foraminifera*	2460 ± 35	1840	1705–1976 (1.0)
NOSAMS-OS-81235[a]	429	*Mixed planktonic foraminifera*	2550 ± 30	1950	1824–2089 (1.0)
NOSAMS-OS-72103[a]	453	*Mixed planktonic foraminifera*	2800 ± 40	2250	2098–2387 (1.0)
NOSAMS-OS-81327[a]	479	*Mixed planktonic foraminifera*	2840 ± 35	2300	2143–2449 (1.0)
NOSAMS-OS-64752[a]	503	*Mixed planktonic foraminifera*	2760 ± 30	2210	2081–2328 (1.0)
NOSAMS-OS-81328[a]	527	*Mixed planktonic foraminifera*	3020 ± 25	2550	2380–2694 (1.0)
NOSAMS-OS-64767[a]	553	*Mixed planktonic foraminifera*	3030 ± 25	2560	2395–2703 (1.0)
NOSAMS-OS-81329[a]	579	*Mixed planktonic foraminifera*	3280 ± 25	2830	2734–2947 (1.0)
NOSAMS-OS-64768[a]	608	*Mixed planktonic foraminifera*	3350 ± 25	2910	2777–3048 (1.0)
NOSAMS-OS-81330[a]	635	*Mixed planktonic foraminifera*	3430 ± 25	3020	2870–3157 (1.0)
NOSAMS-OS-72104[a]	658	*Mixed planktonic foraminifera*	3600 ± 25	3250	3109–3366 (1.0)
NOSAMS-OS-81331[a]	679	*Mixed planktonic foraminifera*	3820 ± 30	3500	3370–3621 (1.0)
NOSAMS-OS-64769[a]	698	*Mixed planktonic foraminifera*	3750 ± 25	3420	3313–3550 (1.0)
NOSAMS-OS-81332[a]	722	*Mixed planktonic foraminifera*	3970 ± 30	3680	3551–3826 (1.0)
NOSAMS-OS-72105[a]	748	*Mixed planktonic foraminifera*	4150 ± 35	3920	3759–4079 (1.0)
NOSAMS-OS-81333[a]	772	*Mixed planktonic foraminifera*	4280 ± 30	4090	3926–4246 (1.0)
NOSAMS-OS-64770[a]	798	*Mixed planktonic foraminifera*	4340 ± 30	4180	4010–4024 (0.001) 4026–4350 (0.989)
NOSAMS-OS-81334[a]	819	*Mixed planktonic foraminifera*	4610 ± 30	4540	4401–4718 (0.992) 4755–4763 (0.008)
NOSAMS-OS-72106[a]	838	*Mixed planktonic foraminifera*	4810 ± 35	4810	4633–4949 (1.0)
NOSAMS-OS-81335[a]	859	*Mixed planktonic foraminifera*	4900 ± 30	4910	4801–5045 (1.0)
NOSAMS-OS-64771[a]	878	*Mixed planktonic foraminifera*	5020 ± 30	5090	4913–5261 (1.0)
NOSAMS-OS-81336[a]	899	*Mixed planktonic foraminifera*	5190 ± 30	5320	5135–5155 (0.010) 5189–5462 (0.990)
NOSAMS-OS-72107[a]	918	*Mixed planktonic foraminifera*	5450 ± 35	5590	5468–5705 (1.0)
NOSAMS-OS-64772[a]	968	*Mixed planktonic foraminifera*	5770 ± 30	5940	5795–5796 (0.001) 5808–5812 (0.002) 5818–6105 (0.097)

[a] Measured at the National Ocean Sciences Accelerator Mass Spectrometry Facility, Woods Hole, United States of America.
[b] Measured at the Keck Carbon Cycle Accelerator Mass Spectrometry Facility, Earth System Science Department, University of California, Irvine, United States of America.
[c] 2σ enclosing 95.4% of probability distribution.
[d] Invalid age for the marine13.14c calibration curve.
[e] A regional reservoir correction (ΔR) of +130 ± 35 years have been applied (Southon et al., 2013).

the CALIB 7.0 software using the MARINE13 calibration dataset (Reimer et al., 2013) with a reservoir correction of 405 years plus an additional 220 ± 40 years (ΔR) to account for older radiocarbon introduced into the surface water by upwelling and for differences between surface and thermocline dwelling foraminifera when using mixed planktonic foraminifera (Southon et al., 2013). The radiocarbon age at 36 cm only consisting of mixed layer dwelling planktonic foraminfera *G. ruber* and *G. sacculifer* was converted to 2σ calendar ages by using the MARINE13 calibration dataset and a mean global reservoir correction of 405 years plus an additional 130 ± 35 years (ΔR; Southon et al., 2013).

A continuous depth-age model was built with a Bayesian approach using the Bacon software (Blaauw and Christen, 2011). This method divides a core into sections and models the accumulation rate for each of these sections. In the following text, all ages refer to calibrated (cal.) years BP.

4.4. Bulk sediment element analysis

We determined the bulk sedimentary element composition of core GeoB10065-7 by X-Ray Fluorescence (XRF). XRF Core Scanner data were collected every 2 cm down-core using a generator setting of 20 kV, 0.087 mA and a sampling time of 20 s directly at the split core surface of the archive half with XRF Core Scanner I at MARUM, University of Bremen. The split core surface was covered with a polypropylene foil to avoid contamination of the XRF measurement unit and desiccation of the sediment. The here reported data have been acquired by XRF Core Scanner I at MARUM using a KEVEX Psi Peltier Cooled Silicon Detector and a KEVEX X-ray Tube 52500008-02 with the target material molybdenum (Mo).

5. Results

5.1. Age control

The three individual depth profiles of radionuclides of the two multi-cores at station GeoB10065-9 (henceforth MUC-A, and MUC-B) and the gravity core at station GeoB10065-7 were depth aligned based on minimizing the sum of squared residuals (Fig. 2; Pittauerova et al., 2009). It was estimated that MUC-A is shifted by 2 cm downwards relative to MUC-B and that there is 20 cm missing on top of gravity core GeoB10065-7 relative to MUC-B. ^{137}Cs values were mostly below the decision threshold and the activity concentrations could only be analyzed from summed up spectra of several sampling intervals. However, unusually high activities of nuclear bomb tests derived isotope ^{241}Am were present and the first appearance of ^{241}Am in depth profiles was used as an additional chronomarker (AD 1950 ± 5 years) in model calculations instead of ^{137}Cs.

The $^{210}Pb_{xs}$ profile between 14 and 32 cm of MUC-A showing an exponential decrease was used for chronology. The Constant Flux-Constant Sedimentation (CF-CS) model (Appleby and Oldfield, 1978) was applied to the investigated profile section with an additional time marker at 29.5 cm based on the first appearance of ^{241}Am. The Constant Rate of Supply (CRS) model (Appleby and Oldfield, 1978), assuming steady flux of $^{210}Pb_{xs}$ and allowing variable sedimentation rates, was applied to the same dataset for comparison. The mean sedimentation rate obtained with the CF-CS model is 0.27 ± 0.02 cm/yr. Sedimentation rates obtained with the CRS model range between 0.23 cm/yr and 0.38 cm/yr with the mean value of 0.28 cm/yr.

The calendar ages calculated from both models show very similar results. The age of the bottom of MUC-A (31.5 cm) was estimated as AD 1942 ± 5 (CF-CS model). Application of both models shows that very recent sediments are likely to be present at 14 cm depth. Within uncertainties of both age models, the calculated ages correspond to AD 2009 ± 7 and AD 2004 ± 6 calendar years, which are close to the day of core recovery (05.09.2005). The $^{210}Pb_{xs}$ data of MUC-A and MUC-B reveal the existence of another 10-cm thick sequence of repeated young sediment above 14 cm. This can likely be attributed to small-scale deformation and/or sliding processes due to seismic activity that can often occur in an earthquake prone region like Indonesia. The monotonous decrease in ^{210}Pb activity of the upper 10 cm would imply a gentle process without mixing of the deformed or re-deposited sediment layer.

The age of the upper 15 cm of GC GeoB10065-7 was calculated using the MUC-A CF-CS model derived sedimentation rate (see above). The gravity core ^{210}Pb chronology of the upper 15 cm extends from AD 1984 ± 6 to AD 1928 ± 5 (Table 1). In order to extend the chronology to deeper parts of sediment profile and estimate the age above a turbidite layer, which occurs in 37–40 cm core depth, the CF-CS model was extrapolated to the depth of 36 cm (above the turbidite layer). This layer would represent year AD 1845 ± 9. The extrapolated ages of the CF-CS model of AD 1881 ± 7 at 27 cm and AD 1845 ± 9 at 36 cm are in good agreement with those obtained from radiocarbon dating of 90 cal yr BP or AD 1859 (2σ age range of AD 1797 and 1950) and of 120 cal yr BP or AD 1828 (2σ age range of AD 1714 and 1910), respectively.

Age control on gravity core GeoB10065-7 below the turbidite layer (37–40 cm depth in core) was established based on 39 AMS radiocarbon measurements (Fig. 3; Table 2). Based on our age model, core GeoB10065-7 covers the last ~6000 years. The age-depth model using the Bayesian approach (Blaauw and Christen, 2011) gives extremely high linear sedimentation rates between 0.11 ± 0.05 cm/yr and 0.35 ± 0.05 cm/yr which are comparable with those obtained from the ^{210}Pb age models (CF-CS model, 0.27 ± 0.02 cm/yr; CRS model, 0.23–0.38 cm/yr; see above).

5.2. Results of bulk sediment element analysis

Fig. 4 shows the titanium (Ti), iron (Fe) and calcium (Ca) XRF intensity data of core GeoB10065-7. The intensities of the Ti are lower between ~6000 yr BP and 3000 yr BP and generally higher after ~3000 BP with a period of lower Ti intensities between ~2000 yr BP and 1000 yr BP (Fig. 4a). The intensities of the terrestrial endmember Fe show the same trend as the Ti intensities (Fig. 4b). The intensities of Fe are also presented in order to demonstrate the coherent changes in the terrestrial endmember elements at our site over the past 6000 years. Increased intensities of Ti and Fe after ~3000 yr BP are interpreted as increased supply of siliciclastic material of fluvial origin. The Ca intensities reveal an inverse relationship to the Ti and Fe intensities with higher intensities between ~6000 yr BP and 3000 yr BP and lower intensities after ~3000 yr BP (Fig. 4c). The ln-ratio of Ti/Ca shows lower values between ~6000 yr BP and 3000 yr BP compared to the last 3000 years, indicating lower riverine detrital supply and hence weaker AISM rainfall during the Mid Holocene compared to the Late Holocene (Fig. 4d). A conspicuous shift towards higher terrestrial sediment supply and thus AISM rainfall occurred at around 2800 yr BP that is followed by a period of increased AISM rainfall between ~1700 yr BP and ~2800 yr BP. The ln-ratio of Ti/Ca exhibit less riverine detrital supply from ~1700 yr BP to ~1200 yr BP (Fig. 4d). Thereafter, the ln-ratio of Ti/Ca exhibits a steady increase in terrestrial supply and hence AISM rainfall to the present after ~1200 yr BP (Fig. 4d).

6. Discussion

Our AISM record bears similarities with Holocene changes in rainfall as inferred from a ln-ratio of Ti/Ca of a core located south off Java (Mohtadi et al., 2011) and a cave stalagmite stable oxygen isotope record from Flores, Indonesia (Griffiths et al., 2009, 2010), which also show a change from a drier Mid Holocene to a wetter Late Holocene (Fig. 5c–d). The southern Indonesian proxy records for changes in AISM rainfall show a similar overall increase in AISM rainfall until ~1200 yr BP, while the development of the AISM rainfall as inferred from these records is inconsistent thereafter (Fig. 5a–d). Our Ti/Ca record suggests a steady increase in AISM rainfall after ~1200 yr BP, while the Flores and the record off southern Java suggest drier conditions (Fig. 5c–d). The steady increase in rainfall after ~1200 yr BP as inferred from our Ti/Ca record is consistent with rainfall reconstructions based on δD of terrestrial plant waxes from Lake Lading (East Java; Konecky et al., 2013, Fig. 5b). We suggest that the overall long-term trend of our record with an increasing AISM rainfall over the Mid-to-Late Holocene resembles high-resolution Southern Hemisphere low latitude monsoon proxy records, e.g. from South America (van

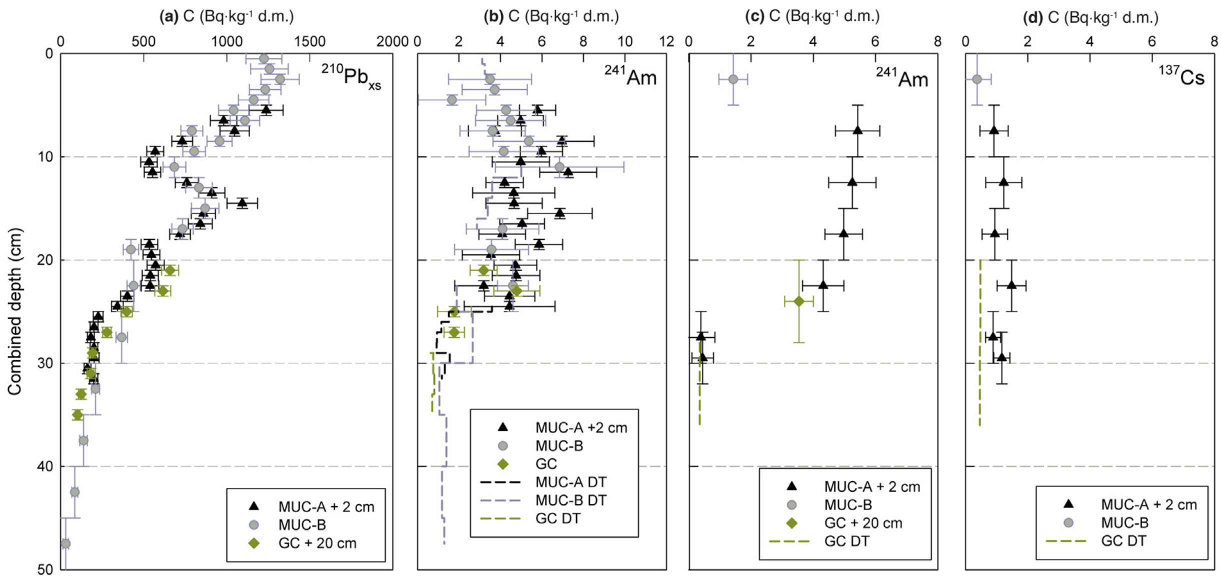

Fig. 2. Depth aligned profiles of radionuclides (a, $^{210}Pb_{xs}$; b, ^{241}Am, c, ^{241}Am summed up; d, ^{137}Cs summed up) measured in sediment cores GeoB10065-9 (MUC-A and MUC-B) and GeoB10065-7 (GC). Horizontal error bars express uncertainties (1σ standard deviation including counting statistics and detector calibration uncertainty), vertical error bars depth limitation of individual samples (a) and (b) or summed up intervals (c) and (d). Values below decision threshold are depicted in dashed line.

Breukelen et al., 2008) and Southeast Africa (Schefuß et al., 2011). This overall increasing trend of the Southern Hemisphere monsoons is in line with orbitally induced rising Southern Hemisphere summer insolation during this interval, indicating that the first-order trend from dry to wet is most likely caused by astronomical forcing (Fig. 5f). Different to the Southern Hemisphere low latitude monsoon proxy records from van Breukelen et al. (2008) and Schefuß et al. (2011) which show a continuous increase in monsoonal rainfall with a continuous increase in austral summer insolation, our AISM rainfall record shows a conspicuous shift in AISM rainfall at around 2800 yr BP and only a minor increase in rainfall between ~6000 yr BP and 2800 yr BP, despite an increase in austral summer insolation around 10 W/m^2 (see Fig. 5a and discussion below). In contrast to the southern Indonesian AISM rainfall records, the Kimberley stalagmite $\delta^{18}O$ record of tropical Western Australia (Denniston et al., 2013, Fig. 5e) reveals an opposite behaviour of monsoonal rainfall with a decreasing AISM rainfall over the Mid-to-Late Holocene (see discussion below).

As demonstrated by Wang et al. (2005) for the Holocene East Asian Summer Monsoon (EASM), monsoon activity is not only affected by long-term, orbitally induced insolation changes but also by changes in solar activity. We tested the influence of solar output

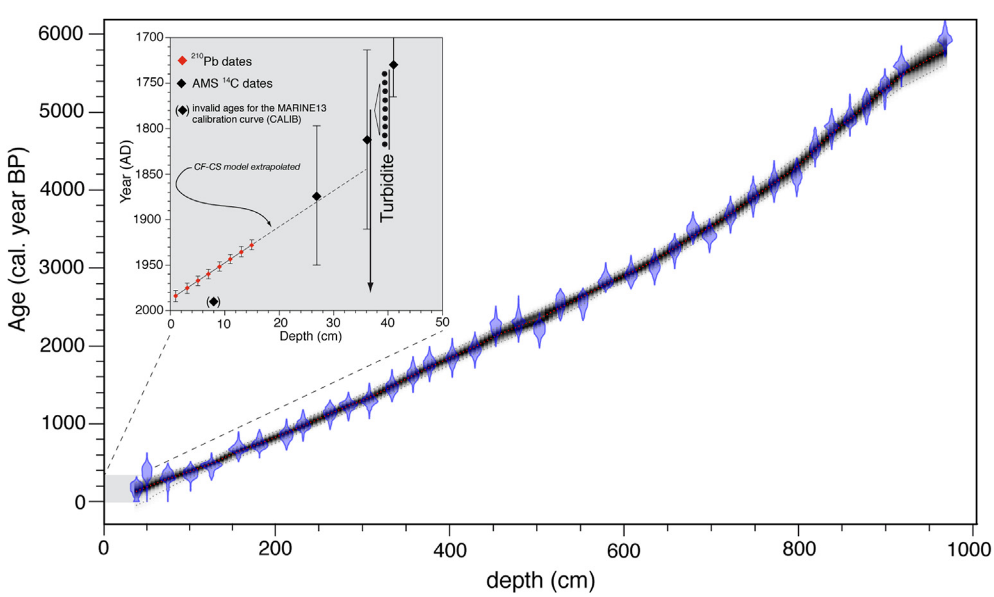

Fig. 3. Age–depth relationship of core 10065-7. Age control on gravity core GeoB10065-7 above the turbiditic layer is based on excess ^{210}Pb, an anthropogenic fallout radionuclide ^{241}Am and two AMS-^{14}C dates. Squares indicate calibrated (cal.) ages with 2σ error bars. The age–depth relationship below the turbiditic layer was built with a Bayesian approach using the Bacon software (Blaauw and Christen, 2011) overlying the distributions of the individual dates (blue). Line curve shows the best model (red dotted line: mean), grey-scales indicate chronological uncertainties (grey dotted lines: the model's 95% probability interval). (For interpretation of the references to colour in this figure legend, the reader is referred to the web version of this article.)

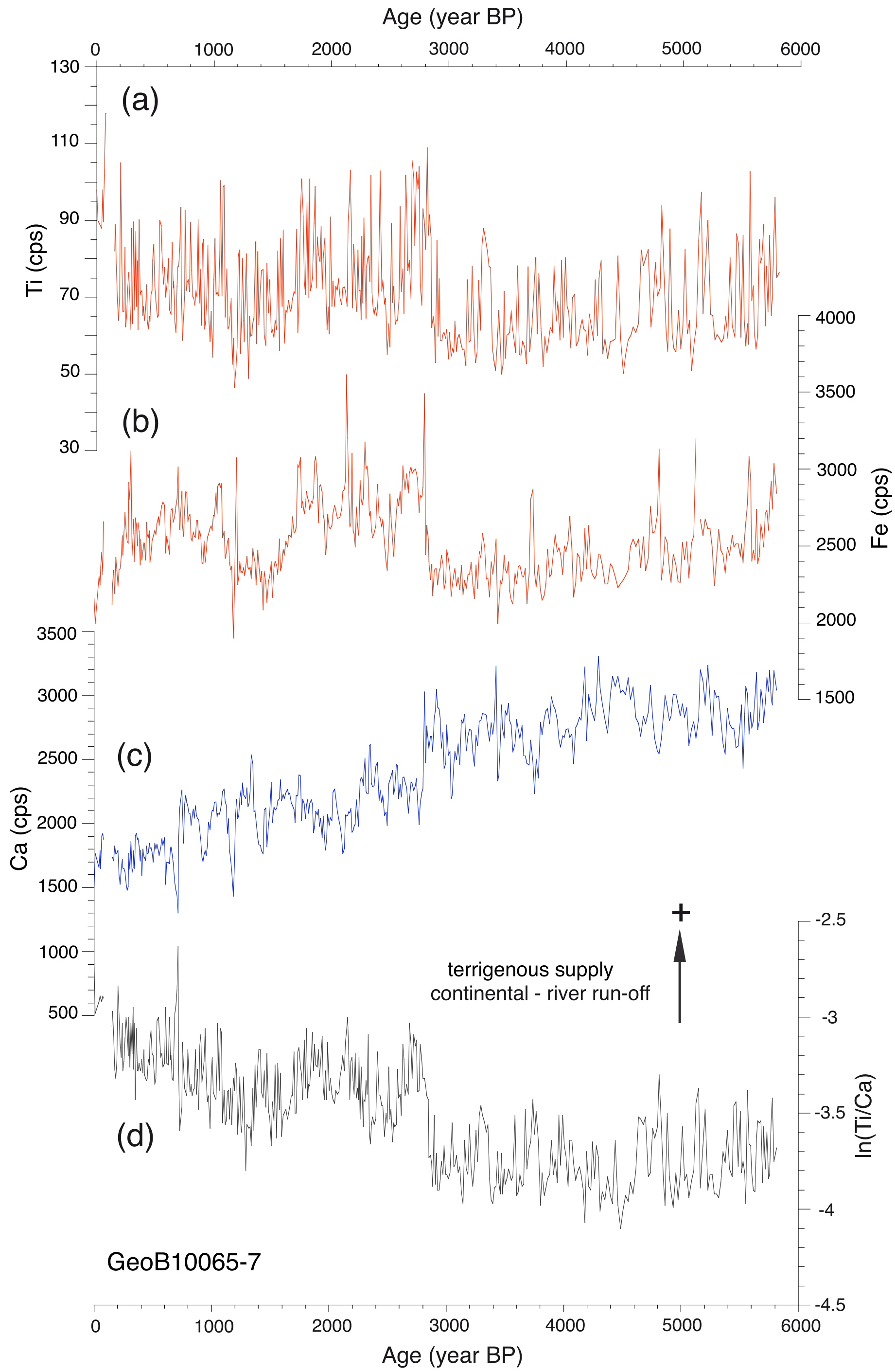

Fig. 4. (a) Titanium (Ti), (b) iron (Fe) and, (c) calcium (Ca) intensity XRF logs in counts per second (cps) of core GeoB10065-7. (d) ln-ratio of Ti/Ca of core GeoB10065-7.

variations on the AISM in an attempt to assess solar activity being important in controlling AISM variability during the Holocene. For that reason, we compared our Ti/Ca record to the sunspot number record of Solanki et al. (2004), a proxy for solar activity (Fig. 6b). Visually, changes in our Ti/Ca record resemble the long-term trend in solar activity with periods of weaker AISM rainfall broadly corresponding to higher solar activity (6000–3000 yr BP), while a strengthened AISM is associated with an overall long-term decrease in solar activity (after 2800 yr BP; Fig. 6a–b). In addition, we find a link between changes in AISM rainfall and solar activity with certain solar minima corresponding to stronger southern Indonesian rainfall, in particular at around 2800 years BP (see Fig. 6a–b). The correlation between the unsmoothed Ti/Ca and solar activity records is relatively low ($r = -0.319$) but statistically significant for the past 6000 years ($p < 0.05$) when taking serial correlation into account (Mudelsee, 2003). The statistical significance of the correlation indicates that some of the variability in the AISM rainfall can be attributed to changes in solar activity (Fig. 6c). Our results suggest that solar forcing plays a role in driving AISM rainfall variability during the past 6000 years, even though the variance in our Ti/Ca record that can be explained by changes in the solar output is small.

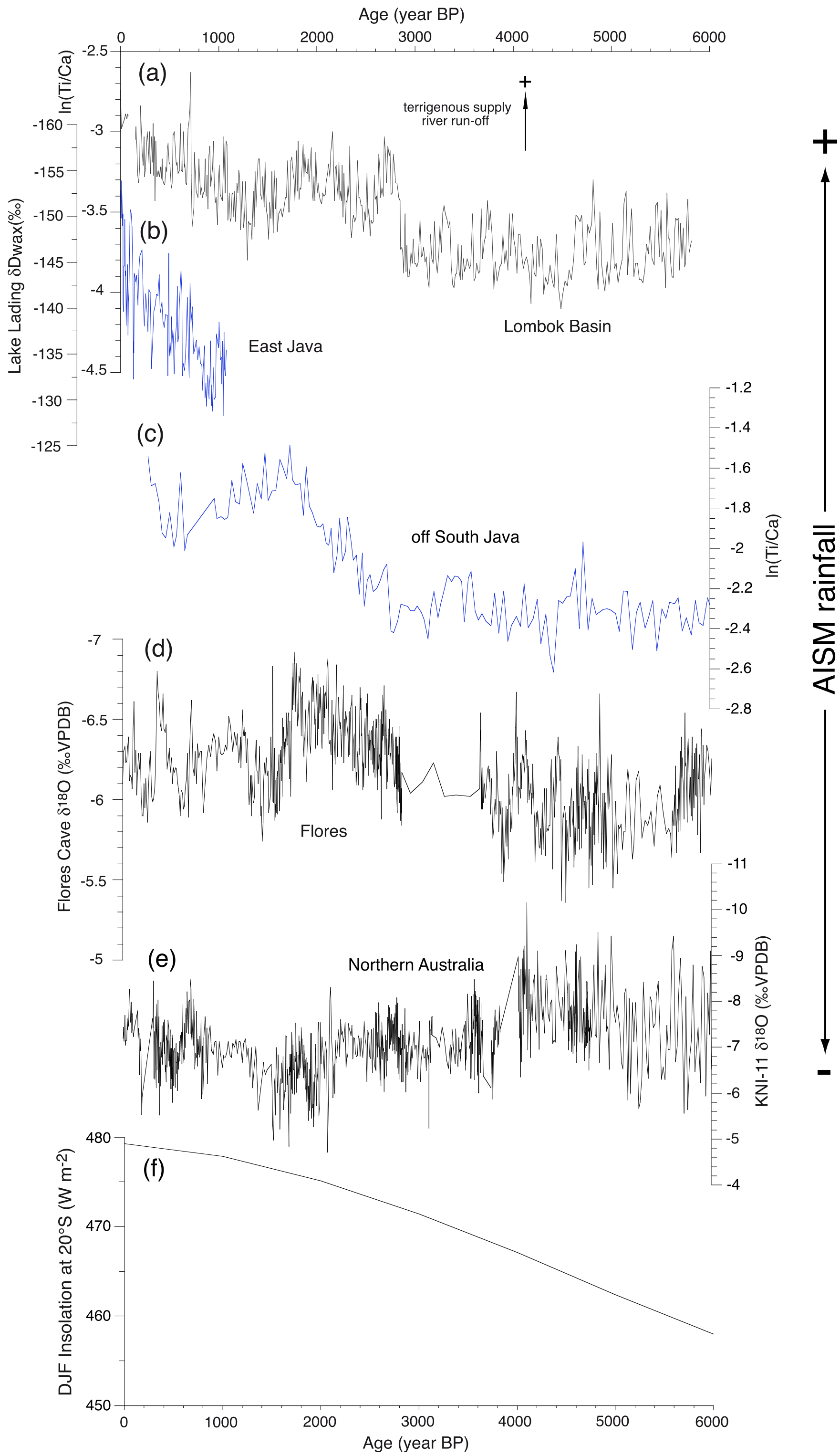

Fig. 5. Proxy records for monsoonal rainfall changes in southern Indonesia and northern Australia. (a) ln-ratio of Ti/Ca in core GeoB10065-7; (b) Lake Lading (East Java) leaf wax δD record (Konecky et al., 2013); (c) ln-ratio of Ti/Ca in core GeoB10053-7 off southern Java (Mohtadi et al., 2011); (d) Liang Luar (Flores) $\delta^{18}O$ record (Griffiths et al., 2010); (e) Eastern Kimberley $\delta^{18}O$ record, tropical Western Australia (Denniston et al., 2013) and (f) Southern Hemisphere (austral) summer insolation (20°S; DJF; Laskar et al., 2004). Site locations are given in Fig. 1.

The most conspicuous shift in terrigenous sediment supply and thus AISM rainfall occurred at around 2800 yr BP, coinciding with one of the strongest grand solar minima of the Holocene (see also above; Solanki et al., 2004; Usoskin et al., 2007). As lower solar radiative forcing is usually associated with less surface ocean evaporation and, consequently, reduced monsoonal rainfall in tropical regions (Meehl et al., 2003), our finding of enhanced rainfall over southern Indonesia during times of reduced solar

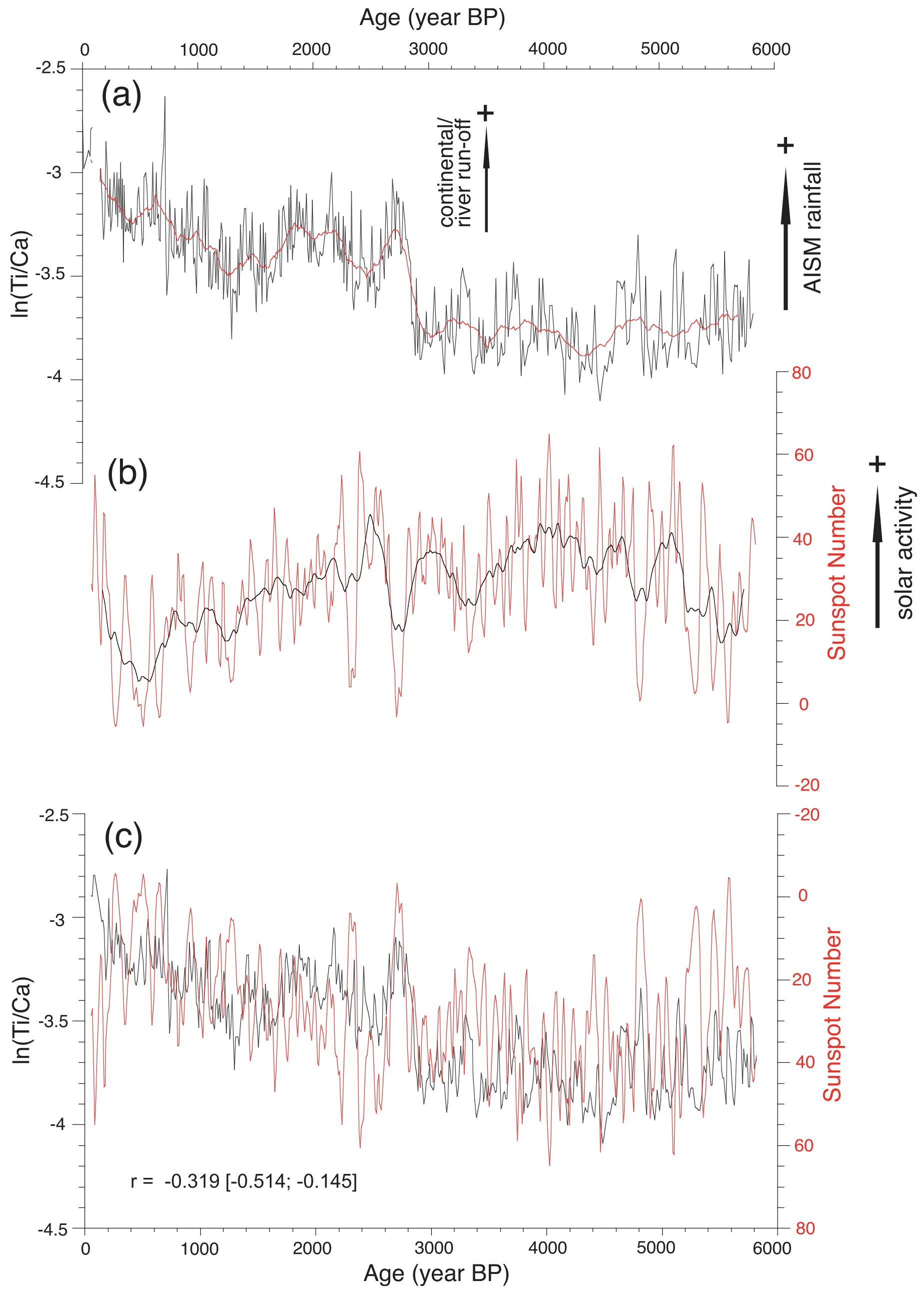

Fig. 6. Changes in AISM rainfall and solar activity. (a) Ti/Ca ratios in core GeoB10065-7; (b) 10-year averaged reconstructed sunspot number (Solanki et al., 2004); (c) 10-year averaged ln-ratios of Ti/Ca (black) and sunspot numbers (red). 95% confidence intervals (in brackets) for the Pearson correlation coefficient (r) were calculated using a non-parametric bootstrap method, where autocorrelation has been taken into account (Mudelsee, 2003). 21-point running means shown in bold (a–b) to illustrate the long-term trends in ln-ratios of Ti/Ca and sunspot numbers. (For interpretation of the references to colour in this figure legend, the reader is referred to the web version of this article.)

activity, in particular the 2800 yr BP grand solar minimum, seems counterintuitive. Moreover, according to the theoretical mechanism of a Pacific Ocean “dynamical thermostat” (Clement et al., 1996; Mann et al., 2005; Marchitto et al., 2010), solar minima should favour El Niño-like conditions and hence drier climate over Indonesia. To find a possible mechanism that could reconcile reduced solar activity with enhanced southern Indonesian summer rainfall, we analyzed the output from an idealized solar sensitivity experiment (Varma et al., 2011) using the coupled climate model CCSM3 (Collins et al., 2006). In this experiment, solar forcing is simply implemented through a change in total solar irradiance (TSI) with no wavelength-dependence and mostly affects the climate system through shortwave absorption by the surface. The TSI has been reduced by 2 Wm^{-2} (corresponding to 0.15%) for a period of 70 years to capture the multi-decadal timescale of typical solar grand minima (Usoskin et al., 2007). In order to enhance statistical significance of the model results, the TSI sensitivity experiment consists of three ensemble members. The resolution of the atmospheric model component is given by T31 (3.75° transform grid) with 26 layers in the vertical (Yeager et al., 2006) and preindustrial boundary conditions were applied (Otto-Bliesner et al., 2006). For a detailed description of the experimental design, the reader is referred to Varma et al. (2011).

In the model experiment, reduced solar forcing causes an overall surface cooling, which is usually less pronounced over the ocean than over land due to greater thermal inertia and the regulating

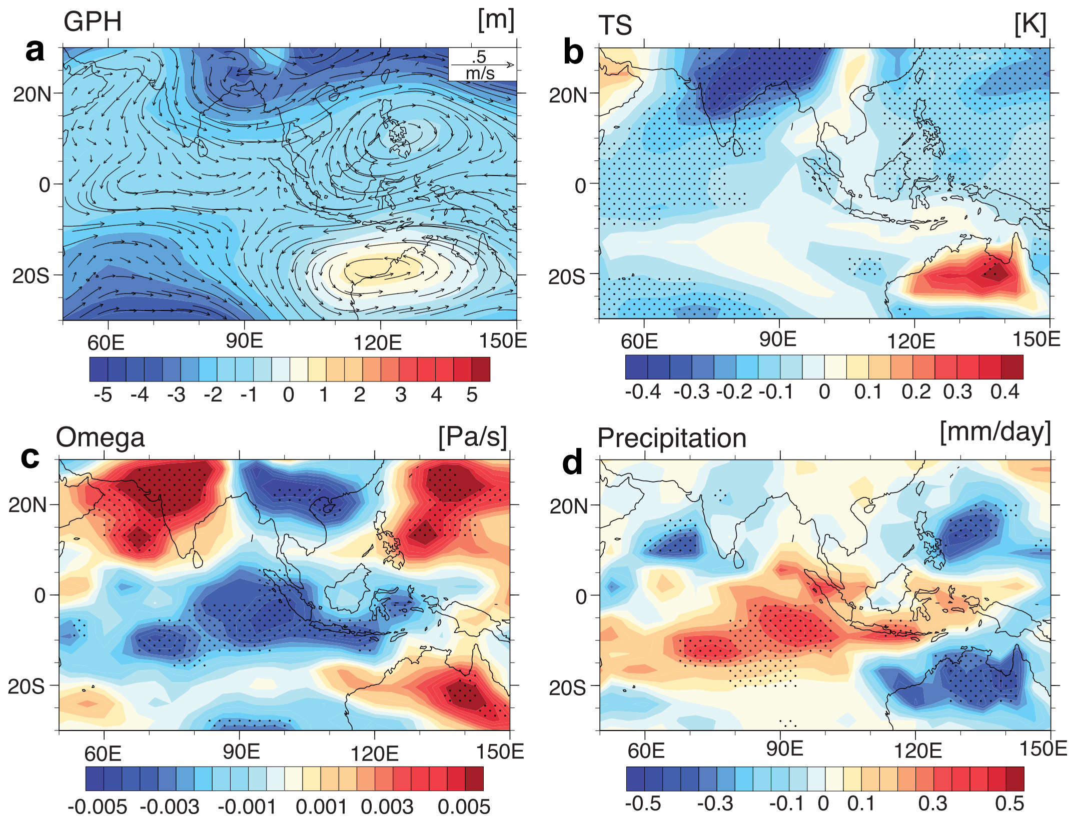

Fig. 7. Climatic response to a multi-decadal (70 years) reduction in total solar irradiance by 2 Wm^{-2} in a coupled climate model (CCSM3). Shown are austral summer (December–February) anomalies (low minus high solar irradiance) in the model ensemble mean averaged over the entire 70-year interval of the solar forcing experiment for (a) 850 hPa geopotential height and 850 hPa wind, (b) surface temperature, (c) vertical velocity at 500 hPa, and (d) precipitation. Stippling in b-d indicates significance of the anomaly at the 0.05 level.

effect of evaporative heat fluxes on sea surface temperature (Meehl et al., 2003). The resulting reduction in sensible heating of air over land and in the land-sea thermal contrast in combination with a decrease in surface ocean evaporation lowers the monsoonal moisture influx to northern Australia and precipitation there. The resulting decrease in latent heat release from precipitation further leads to a substantial weakening of the Australian monsoon trough and slowing of the associated winds (Fig. 7a) and upward motion of air (Webster et al., 1998; Meehl et al., 2003, Fig. 7c). Consequently, even less moisture is advected towards northern Australia creating a positive feedback (Levermann et al., 2009). Reduced evapotranspiration from the drier land surface and less cloudiness (not shown) eventually cause a net surface warming over northern Australia (Fig. 7b). In the northern part of the large-scale austral summer Asian-Australian monsoon system, strong cooling over cloud-free India is associated with enhanced subsidence (Fig. 7c), accelerating the curved low-level circulation from India towards Indonesia via the western Indian Ocean (Fig. 7a). Between the Australian and Indian anomalies of downward vertical motion (Fig. 7c), anomalous low-level wind convergence (Fig. 7a) and ascent (Fig. 7c) takes place, leading to higher rainfall over southern Indonesia and the south-equatorial eastern Indian Ocean in response to a solar minimum (Fig. 7d). The associated release of latent heat acts as a positive feedback on the wind circulation anomaly (Gill, 1980). The simulated fractional change in precipitation over this area is roughly 5–10%, which is of the same order of magnitude as the projected austral summer rainfall increase across southern Indonesia until the end of the 21st century as derived from a multi-model average forced by rising greenhouse gas concentrations (Christensen et al., 2007). This quantitative comparison, however, must be taken with care and can only provide a very crude estimate of the solar impact. First, the true magnitude of past TSI variations may differ from the TSI reduction applied in the CCSM3 sensitivity experiment. Even though a TSI reduction of 2 Wm^{-2} is consistent with physics-based estimates of the extremest solar variations during the Late Holocene according to Steinhilber et al. (2009), it can be considered a relatively strong forcing which has been chosen to enhance the detectability of the climatic response in the model. We acknowledge that there are substantial uncertainties in the estimates of the magnitude of past TSI variability (Lockwood, 2011; Judge et al., 2012). Secondly, the CCSM3 simulations do not include potential amplifying mechanisms of solar forcing associated with charged particle effects or changes in stratospheric ozone due to solar ultraviolet variability (cf. Gray et al., 2010). In summary, while lacking “top–down processes” (e.g. Meehl et al., 2009), the idealized CCSM3 solar sensitivity experiment provides a physically-consistent mechanism which may explain the counterintuitive proxy-derived result of enhanced AISM rainfall in southern Indonesia in response to reduced solar output. The model highlights the importance of feedbacks associated with moisture fluxes and latent heat release in the monsoonal system. In particular, the suggested mechanism of solar-forced variations in AISM rainfall is independent from ENSO conditions in the equatorial Pacific (cf. Marchitto et al., 2010; see discussion below).

There are two remarkable features associated with the suggested mechanism of solar-forced variations on AISM rainfall. First, the 2800 yr BP solar minimum is associated with an outstanding shift in our AISM rainfall record, whereas other grand solar mimima are less pronounced in the Ti/Ca record, e.g. the minimum around

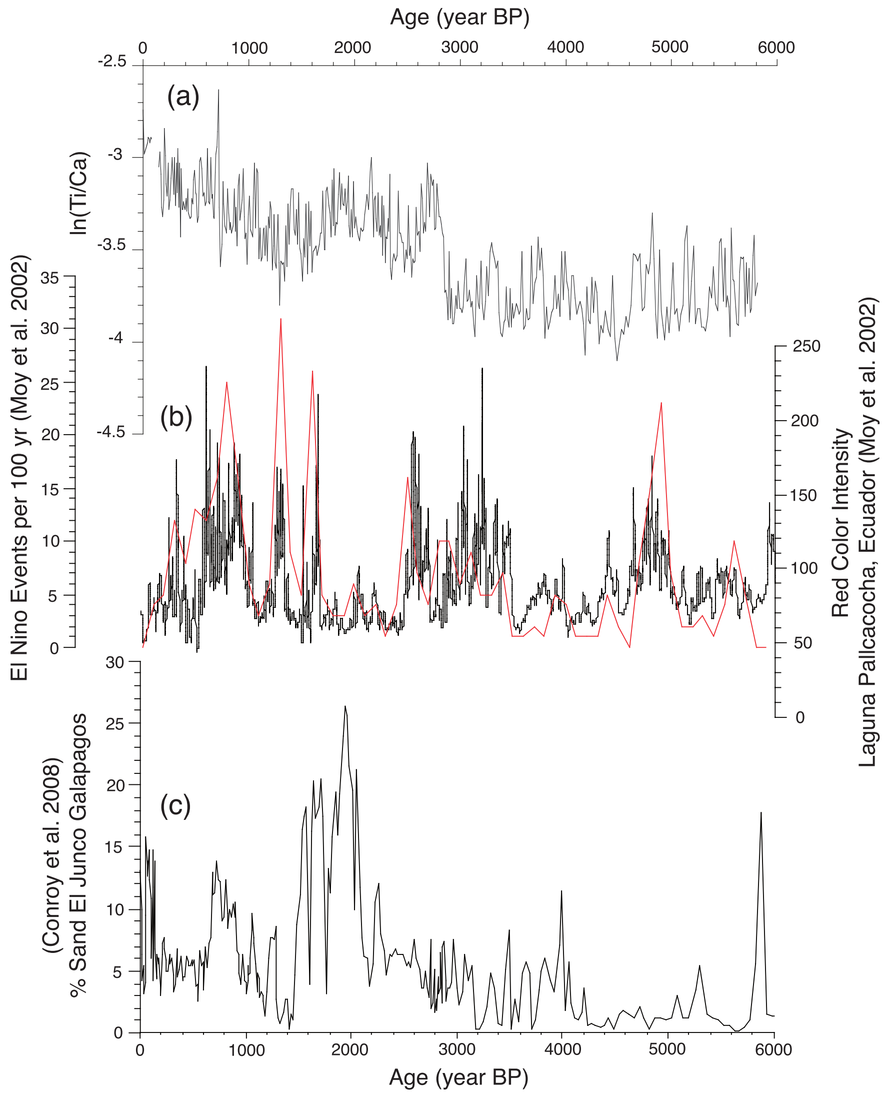

Fig. 8. Proxy records for rainfall variability in southern Indonesia and the eastern equatorial Pacific (EEP): (a) ln-ratios of Ti/Ca in core GeoB10065-7 (this study), (b) red color intensity (proxy for terrestrial runoff) in Laguna Pallcacocha in Ecuador and El Niño events per 100 yr in red (Moy et al., 2002), and (c) percent sand in El Junco Lake in the Galapagos Islands indicative of ENSO frequency (Conroy et al., 2008). (For interpretation of the references to colour in this figure legend, the reader is referred to the web version of this article.)

5200 yr BP (Fig. 6c). Second, our AISM record indicates that the strengthening of the southern Indonesian rainfall during the 2800 yr BP grand solar minimum represents a distinct shift towards overall wetter conditions thereafter (Fig. 5a).

Why the 2800 years BP event stands out so drastically in our monsoon record as well as in other records (see below), can currently not be answered conclusively. We suggest that in contrast to other solar minima, the 2800 yr BP minimum lasted longer than most other solar minima. This might have resulted in a stronger effect on the climate system, and also facilitates the detection in proxy records. Either way, there is clear evidence that the 2800 yr BP solar minimum affected climate conditions over much of the planet, including shifts of the Southern Westerlies (van Geel et al., 2000), the establishment of modern wind regimes in northern Africa (Kröpelin et al., 2008), and shifts in atmospheric circulation over Europe (Martin-Puertas et al., 2012). Moreover, the Dongge Cave EASM record displays a decrease in rainfall around 2800 years BP but no change during other big events in solar output between 4000 years BP and 6000 years BP (Wang et al., 2005).

In order to explain the generally higher rainfall levels after the 2800yr BP event we suggest that the combined effect of orbital and solar forcing is responsible for the long-term temporal behaviour of AISM rainfall over southern Indonesia as well as northern Australia. Despite an increase in austral summer insolation around 10 W/m^2 between 6000 yr BP and 3000 yr BP, only a minor increase in AISM rainfall occurred between ~6000 yr BP and 2800 yr BP. We suggest that a long-term upward trend in solar output between 6000 yr BP and ~4000 yr BP (Fig. 6b) counteracts increasing orbital forcing such that the long-term trend in the Ti/Ca record is minor (Fig. 6a). After the 2800 yr BP event, enhanced orbital forcing keeps rainfall at a generally higher level than during the drier Mid Holocene. After ~1200 yr BP decreasing solar activity causes rainfall to increase further for about 1000 years (Fig. 5a). The steady increase in rainfall after ~1200 yr BP is consistent with rainfall reconstructions based on δD of terrestrial plant waxes from Lake Lading (East Java; Konecky et al., 2013, Fig. 5b).

As over the entire period solar activity explains only a small but statistically significant fraction of the monsoonal rainfall variations, internal climate variability and/or volcanic forcing involving climatic teleconnections may probably explain another portion of the high frequency variations over the entire Ti/Ca record. However, there is no evidence of any substantial volcanic forcing during the 2800 yr BP event (Zielinski et al., 1997). In modern climatology, rainfall in Indonesia is highly sensitive to ENSO variability with El Niño events typically resulting in reduced rainfall and subsequent drought (Aldrian and Susanto, 2003). To assess whether changes in the background state of the tropical Pacific, so-called "El Niño–like" or "La Niña–like" conditions, have contributed to the Holocene AISM rainfall variability, we compare our ln-ratio Ti/Ca record with lake sedimentary records from Laguna Pallchachoca in Ecuador (Moy et al., 2002) and the El Junco Crater Lake in the Galapagos Islands (Conroy et al., 2008) which represent local rainfall intensity and, hence, are indicative of past El Niño events (Fig. 8). It is expected that more frequent and/or intense El Niño events have resulted in reduced rainfall and subsequent drought in the AISM region and, consequently, less riverine terrestrial supply to our site. Comparison of our Ti/Ca record with the lake sedimentary records from Ecuador (Moy et al., 2002) and the Galapagos Islands (Conroy et al., 2008) shows no correlation [$r = -0.089$ with 95% confidence interval (−0.296; 0.134)] and a high covariance [$r = 0.481$ with 95% confidence interval (0.237; 0.605)], respectively. However, despite the high covariance, comparison of our Ti/Ca record with the El Junco Crater Lake in the Galapagos Islands (Conroy et al., 2008) reveals that periods of more frequent and/or intense El Niño events after ~3000 yr BP (Conroy et al., 2008) are associated with increased terrigenous supply and thus enhanced AISM rainfall (Fig. 8). However, since El Niño events cause reduced rainfall and subsequent drought in the AISM region, the positive correlation between El Niño events and southern Indonesian rainfall, in particular after ~3000 yr BP, does not imply a causal relationship, but perhaps a common forcing. Moreover, with no clear evidence of El Niño events covarying with La Niña events on that time scales, which typically result in increased rainfall over central and southern Indonesia and northern Australia (Aldrian and Susanto, 2003), we cannot attribute higher supply of terrigenous material and changes in AISM rainfall to more La Niña events after ~3000 yr BP. Based on a stalagmite record from tropical Australia however, it was argued that more stronger El Niño events may have played a dominant role in driving AISM variability since at least the middle Holocene (Denniston et al., 2013). We emphasize that rainfall variability in tropical northern Australia is not only in conflict with our Ti/Ca record for changes in AISM rainfall variability but also with the Ti/Ca record off south Java (Mohtadi et al., 2011) and the Flores cave stalagmite record (Griffiths et al., 2009, 2010).

Our model simulation which reveals a distinct contrast in rainfall over southern Indonesia and northern Australia during solar minima (Fig. 7d) may also help to reconcile this apparent contradiction between the northern Australian and southern Indonesian records of AISM variability since the middle Holocene (~4000–3000 yr BP). The increased AISM rainfall between e.g. ~1500 yr BP and 2800 yr BP as inferred from our Ti/Ca record is consistent with higher precipitation as recorded in the Flores stalagmite stable oxygen isotope record (Griffiths et al., 2009, 2010), while northern Australia shows a trend of decreasing rainfall during that time period (Denniston et al., 2013; see also above). It was argued that more stronger El Niño events may have played a dominant role in this reduction of northern Australian precipitation (Denniston et al., 2013). However, this scenario is in conflict with the modern climatology in the region as El Niño events are also typically associated with reduced rainfall and subsequent drought in central and southern Indonesia (e.g. Aldrian and Susanto, 2003; see discussion below). Thus, we hypothesize that after the 2800 yr BP event a general decrease in solar activity favoured an increase in rainfall in southern Indonesia while northern Australia experienced a reduction in rainfall. In order to better assess the role of ENSO on rainfall over the Maritime Continent on longer timescales other, annually resolved and thus more ENSO-sensitive archives such as varves, tree rings or corals are required. Such archives will help quantifying the extent of ENSO impact on rainfall in time and space but not yet available from the Maritime Continent.

7. Conclusions

In the light of our new record and previously published data from the Northern Hemisphere Indian and East Asian monsoon (Fleitmann et al., 2003; Gupta et al., 2005; Wang et al., 2005; Zhang et al., 2008), a picture emerges suggesting that the Asian-Australian monsoon system as a whole is responding to variations in the solar output. The combined effect of orbital and solar forcing explains important details in the temporal behaviour of AISM rainfall over southern Indonesia during the last 6000 years. The comparison with El Niño proxy records suggests that El Niño did not exert a significant control on AISM rainfall variability at multi-decadal to multi-millennial timescales over the last 6000 years. In addition, the contrasting patterns in rainfall variability over southern Indonesia and northern Australia require further investigations.

Acknowledgements

S. Steinke and M. Mohtadi acknowledge financial support from the Deutsche Forschungsgemeinschaft (DFG grants STE1044/4-1 and HE3412/15-1) and the German Bundesministerium für Bildung und Forschung (BMBF grant PABESIA). We thank J. Southon and D. Oppo for valuable comments on the age model and on an earlier draft of the manuscript, U. Röhl and V. Lukies for technical support, and K. B. Olafsdottir for statistical analyses. This research used data acquired at the XRF Core Scanner Lab at the MARUM – Center for Marine Environmental Sciences, University of Bremen, Germany. We thank three anonymous reviewers for their constructive criticisms that have helped to improve the manuscript.

References

Adler, R.F., 13 others, 2003. The version-2 Global Precipitation Climatology Project (GPCP) monthly precipitation analysis (1979-present). J. Hydrometeorol. 4, 1147–1167. http://dx.doi.org/10.1175/1525-7541(2003)004<1147:TVGPCP>2.0.CO;2.

Aldrian, E., Susanto, R., 2003. Identification of three dominant rainfall regions within Indonesia and their relationship to sea surface temperature. Int. J. Clim. 23, 1435–1452.

Appleby, P.G., Oldfield, F., 1978. The calculation of lead-210 dates assuming a constant rate of supply of unsupported ^{210}Pb to the sediment. Catena 5, 1–8.

Blaauw, M., Christen, J.A., 2011. Flexible paleoclimate age–depth models using an autoregressive gamma process. Bayesian Anal. 6 (3), 457–474. http://dx.doi.org/10.1214/11-BA618.

Christensen, J.H., 16 others, 2007. Regional Climate Projections. In: Solomon, S., 7 others (Eds.), Climate Change 2007. The Physical Science Basis. Contribution of Working Group I to the Fourth Assessment Report of the Intergovernmental Panel on Climate Change. Cambridge University Press, Cambridge, United Kingdom and New York, NY, USA, pp. 848–940.

Clement, A.C., Seager, R., Cane, M.A., Zebiak, S.E., 1996. An ocean dynamical thermostat. J. Clim. 9, 2190–2196 doi:10.1175/15200442(1996)009<2190:AODT<2.0.CO;2.

Collins, W.D., 14 others, 2006. The community climate system model version 3 (CCSM3). J. Clim. 19, 2122–2143. http://dx.doi.org/10.1175/JCLI3761.1.

Conroy, J.L., Overpeck, J.T., Cole, J.E., Shanahan, T.M., Steinitz-Kannan, M., 2008. Holocene changes in eastern tropical Pacific climate inferred from Galapagos lake sediment record. Quat. Sci. Rev. 27, 1166–1180.

Denniston, 13 others, 2013. A stalagmite record of Holocene Indonesian–Australian summer monsoon variability from the Australian tropics. Quat. Sci. Rev. 78, 155–178.

Fleitmann, D., Burns, S.J., Mudelsee, M., Neff, U., Kramers, J., Mangini, A., Matter, A., 2003. Holocene forcing of the Indian monsoon recorded in a stalagmite from Southern Oman. Science 300, 1737–1739. http://dx.doi.org/10.1126/science.1083130.

Gill, A.E., 1980. Some simple solutions for heat-induced tropical circulation. Q. J. Roy. Meteor. Soc. 106, 447–462.

Gray, L.J., Beer, J., Geller, M., Haigh, J.D., Lockwood, M., Matthes, K., Cubasch, U., Fleitmann, D., Harrison, G., Hood, L., Luterbacher, J., Meehl, G.A., Shindell, D., van Geel, B., White, W., 2010. Solar influences on climate. Rev. Geophys. 48. http://dx.doi.org/10.1029/2009RG000282.

Griffiths, M.L., 12 others, 2009. Increasing Australian–Indonesian monsoon rainfall linked to early Holocene sea-level rise. Nat. Geosci. 2, 636–639. http://dx.doi.org/10.1038/NGEO605.
Griffiths, M.L., 10 others, 2010. Evidence for Holocene changes in Australian–Indonesian monsoon rainfall from stalagmite trace element and stable isotope ratios. Earth Planet. Sci. Lett. 292, 27–38. http://dx.doi.org/10.1016/j.epsl.2010.01.002.
Gupta, A.K., Das, M., Anderson, D.M., 2005. Solar influence on the Indian summer monsoon during the Holocene. Geophys. Res. Lett. 32, L17703. http://dx.doi.org/10.1029/2005GL022685.
Hebbeln, D., Jennerjahn, T., Mohtadi, et al., 2006. Report and preliminary results of RV SONNE cruise So-184, Pabesia, Durban (South Africa) – Cilacap (Indonesia)-Darwin (Australia), July 8th – September 13th, 2005. Berichte, Fachbereich Geowissenschaften, Universität Bremen, No. 246, Bremen, 142 pp.
Jennerjahn, T.C., Ittekkot, V., Klöpper, S., Adi, S., Nugroho, S.P., Sudiana, N., Yusmal, A., Prihartanto, Gaye-Haake, B., 2004. Biogeochemistry of a tropical river affected by human activities in its catchment: Brantas River estuary and coastal waters of Madura Strait, Java, Indonesia. Est. Coast. Shelf Sci. 60, 503–514. http://dx.doi.org/10.1016/j.ecss.2004.02.008.
Judge, P.G., Lockwood, G.W., Radick, R.R., Henry, G.W., Shapiro, A.I., Schmutz, W., Lindsey, C., 2012. Confronting a solar irradiance reconstruction with solar and stellar data (Research Note). Astron. Astrophys. 44. http://dx.doi.org/10.1051/0004-6361/201218903.
Kalnay, E., 21 other, 1996. The NCEP/NCAR 40-year reanalysis project. B. Am. Meteorol. Soc. 77, 437–470.
Konecky, B.L., Russell, J.M., Rodysill, J.R., Vuille, M., Bijaksana, S., Huang, Y., 2013. Intensification of southwestern Indonesian rainfall over the past millennium. Geophys. Res. Lett. 40. http://dx.doi.org/10.1029/2012GL054331.
Kröpelin, S., 14 others, 2008. Climate-driven ecosystem succession in the Sahara: the past 6000 years. Science 320, 765–768. http://dx.doi.org/10.1126/science.1154913.
Laskar, J., Robutel, P., Joutel, F., Gastineau, M., Correia, A.C.M., Levard, B., 2004. A long-term numerical solution for the insolation quantities of the Earth. Astron. Astrophys. 428, 261–285.
Levermann, A., Schewe, J., Petoukhov, V., Held, H., 2009. Basic mechanism for abrupt monsoon transitions. Proc. Natl. Acad. Sci. U. S. A. 106, 20572–20577. http://dx.doi.org/10.1073/pnas.0901414106.
Liu, Z., Otto-Bliesner, B., Kutzbach, J., Li, L., Shields, C., 2003. Coupled climate simulation of the evolution of global monsoons in the Holocene. J. Clim. 16, 2472–2490.
Lockwood, M., 2011. Shining a light on solar impacts. Nat. Clim. Change 1, 98–99. http://dx.doi.org/10.1038/nclimate1096.
Magee, J.W., Miller, G.H., Spooner, N.A., Questiaux, D., 2004. Continuous 150 k.y. monsoon record from Lake Eyre, Australia: insolation-forcing implications and unexpected Holocene failure. Geology 32, 885–888. http://dx.doi.org/10.1130/G20672.1.
Mann, M.E., Cane, M.A., Zebiak, S.E., Clement, A., 2005. Volcanic and solar forcing of the tropical Pacific over the past 1000 years. J. Clim. 18, 447–456.
Marchitto, T.M., Muscheler, R., Ortiz, J.D., Carriquiry, J.D., van Geen, A., 2010. Dynamical response of the tropical Pacific Ocean to solar forcing during the early Holocene. Science 330, 1378–1381. http://dx.doi.org/10.1126/science.1194887.
Martin-Puertas, C., Matthes, K., Brauer, A., Muscheler, R., Hansen, F., Petrick, C., Aldahan, A., Possnert, G., van Geel, B., 2012. Regional atmospheric circulation shifts induced by a grand solar minimum. Nat. Geosci. 5, 397–401. http://dx.doi.org/10.1038/NGEO1460.
Meehl, G.A., Washington, W.M., Wigley, T.M.L., Arblaster, J.M., Dai, A., 2003. Solar and greenhouse gas forcing and climate response in the twentieth century. J. Clim. 16, 426–444 doi:10.1175/1520-0442(2003)016<0426:SAGGFA>2.0.CO;2. doi:10.1038/NGEO1460.
Meehl, G.A., Arblaster, J.M., Matthes, K., Sassi, F., van Loon, H., 2009. Amplifying the Pacific climate system response to a small 11-year solar cycle forcing. Science 325, 1114–1118. http://dx.doi.org/10.1126/science.1172872.
Miller, G., Mangan, J., Pollard, D., Thompson, S., Felzer, B., Magee, J., 2005. Sensitivity of the Australian Monsoon to insolation and vegetation: implications for human impact on continental moisture balance. Geology 33, 65–68. http://dx.doi.org/10.1130/G21033.1.
Mohtadi, M., Oppo, D.W., Steinke, S., Stuut, J.-B.W., De Pol-Holz, R., Hebbeln, D., Lückge, A., 2011. Glacial to Holocene swings of the Australian–Indonesian monsoon. Nat. Geosci. 4, 540–544. http://dx.doi.org/10.1038/NGEO1209.
Moy, C.M., Seltzer, G.O., Rodbell, D.T., Anderson, D.M., 2002. Variability of El Nino/Southern oscillation activity at millennial timescales during Holocene epoch. Nature 420, 162–165.
Mudelsee, M., 2003. Estimating Pearson's correlation coefficient with bootstrap confidence interval from serially dependent time series. Math. Geol. 35, 651–665.
Nott, J., Price, D., 1994. Plunge pools and paleoprecipitation. Geology 22, 1047–1050 doi:10.1130/0091-7613(1994)022<1047:PPAP>2.3.CO;2.
Otto-Bliesner, B.L., Thomas, R., Brady, E.C., Ammannm, C., Kothavala, Z., Clauzet, G., 2006. Climate sensitivity of moderate- and low-resolution versions of CCSM3 to preindustrial forcings. J. Clim. 19, 2567–2583. http://dx.doi.org/10.1175/JCLI3754.1.
Pittauerova, D., Fischer, H.W., Mulitza, S., 2009. Using ^{210}Pb and ^{137}Cs record for matching sediment cores. In: International Topical Conference on Polonium and Radioactive Lead Isotopes, Seville, Spain.
Reimer, P.J., et al., 2013. INTCAL13 and MARINE13 radiocarbon age calibration curves, 0–50,000 years cal BP. Radiocarbon 55, 1869–1887 http://dx.doi.org/10.2458/azu_js_rc.55.16947.
Rixen, T., Ittekot, V., Herunadi, B., Wetzel, P., Maier-Reimer, E., Gaye-Haake, B., 2006. ENSO-driven carbon see saw in the Indo-Pacific. Geophys. Res. Lett. 33, L07606. http://dx.doi.org/10.1029/2005GL024965.
Schefuß, E., Kuhlmann, H., Mollenhauer, G., Prange, M., Pätzold, J., 2011. Forcing of wet phases in southeast Africa over the past 17,000 years. Nature 480, 509–512. http://dx.doi.org/10.1038/nature10685.
Solanki, S.K., Usoskin, I.G., Kromer, B., Schüssler, M., Beer, J., 2004. Unusual activity of the Sun during recent decades compared to the previous 11,000 years. Nature 431, 1084–1087. http://dx.doi.org/10.1038/nature02995.
Southon, J., Mohtadi, M., De Pol-Holz, R., 2013. Planktonic foram dates from the Indonesian arc: marine ^{14}C reservoir ages and a mythical AD 535 eruption of Krakatau. Radiocarbon 55, 1164–1172.
Steinhilber, F., Beer, J., Fröhlich, C., 2009. Total solar irradiance during the Holocene. Geophys. Res. Lett. 36, L19704. http://dx.doi.org/10.1029/2009GL040142.
Tierney, J.E., Oppo, D.W., Rosenthal, Y., Russell, J.M., Linsley, B.K., 2010. Coordinated hydrological regimes in the Indo-Pacific region during the past two millennia. Paleoceanography 25. http://dx.doi.org/10.1029/2009PA001871.
Usoskin, I.G., Solanki, S.K., Kovaltsov, G.A., 2007. Grand minima and maxima of solar activity: new observational constraints. Astron. Astrophys. 471, 301–309. http://dx.doi.org/10.1051/0004-6361:20077704.
van Breukelen, M.R., Vonhof, H.B., Hellstrom, J.C., Wester, W.C.G., Kroon, D., 2008. Fossil dripwater in stalagmites reveals Holocene temperature and rainfall variation in Amazonia. Earth Planet. Sci. Lett. 275, 54–60. http://dx.doi.org/10.1016/j.epsl.2008.07.060.
van Geel, B., Heusser, C.J., Renssen, H., Schuurmans, J.E., 2000. Climatic change in Chile at around 2700 BP and global evidence for solar forcing: a hypothesis. Holocene 10, 659–664. http://dx.doi.org/10.1191/09596830094908.
Varma, V., Prange, M., Lamy, F., Merkel, U., Schulz, M., 2011. Solar-forced shifts of the Southern HemisphereWesterlies during the Holocene. Clim. Past. 7, 339–347. http://dx.doi.org/10.5194/cp-7-339-2011.
Wang, Y., Cheng, H., Edwards, R.L., He, Y., Kong, X., An, Z., Wu, J., Kelly, M.J., Dykoski, C.A., Li, X., 2005. The Holocene Asian Monsoon: links to solar changes and North Atlantic climate. Science 308, 854–857.
Webster, P.J., Magaña, V.O., Palmer, T.N., Shukla, J., Tomas, R.A., Yanai, M., Yasunari, T., 1998. Monsoons: processes, predictability, and the prospects for prediction. J. Geophys. Res. 103, 14451–14510.
Yeager, S.G., Shields, C.A., Large, W.G., Hack, J.J., 2006. The low-resolution CCSM3. J. Clim. 19, 2545–2566.
Zhang, P., 16 others, 2008. A test of climate, sun, and culture relationships from an 1810-year Chinese cave record. Science 322, 940–942. http://dx.doi.org/10.1126/science.1163965.
Zielinski, G.A., Mayewski, P.A., Meeker, L.D., Grönvold, K., Germani, M.S., Whitlow, S., Twickler, M.S., Taylor, K., 1997. Volcanic aerosol records and tephrochronology of the Summit, Greenland, ice cores. J. Geophys. Res. 102, 26625–26640.